Title

Combined Assessment of Pulmonary Ventilation and Perfusion with Single-Energy Computed Tomography and Image Processing

Journal

Academic Radiology, 28(5)

ISSN

1076-6332

Authors

Fujita, Yukio
Kent, Michael
Wisner, Erik
et al.

Publication Date

2021-05-01

DOI

10.1016/j.acra.2020.04.004

Peer reviewed

HHS Public Access

Author manuscript

Acad Radiol. Author manuscript; available in PMC 2022 May 01.

Published in final edited form as:

Acad Radiol. 2021 May ; 28(5): 636–646. doi:10.1016/j.acra.2020.04.004.

Combined assessment of pulmonary ventilation and perfusion with single-energy computed tomography and image processing

Yukio Fujita,
Department of Radiation Sciences, Komazawa University, Setagaya, Tokyo 259-1193, Japan

Michael Kent,
Department of Surgical & Radiological Sciences, University of California Davis School of Veterinary Medicine, Davis, California 95616

Erik Wisner,
Department of Surgical & Radiological Sciences, University of California Davis School of Veterinary Medicine, Davis, California 95616

Lynelle Johnson,
Department of Medicine & Epidemiology, University of California Davis School of Veterinary Medicine, Davis, California 95616

Joshua Stern,
Department of Medicine & Epidemiology, University of California Davis School of Veterinary Medicine, Davis, California 95616

Lihong Qi,
Department of Public Health Sciences, University of California Davis, Davis, California 95616

John Boone,
Department of Radiology, University of California Davis School of Medicine, Sacramento, California 95817

Tokihiro Yamamoto
Department of Radiation Oncology, University of California Davis School of Medicine, Sacramento, California 95817

Abstract

Rationale and Objectives—To establish a proof-of-principle for combined assessment of pulmonary ventilation and perfusion using single-energy computed tomography (CT) and image processing/analysis (denoted as single-energy CT ventilation/perfusion imaging).

Materials and Methods—Breath-hold CT scans were acquired at end-expiration and end-inspiration before injection of iodinated contrast agents, and repeated at end-inspiration after contrast injection for 17 canines (8 normal and 9 diseased lung subjects). Ventilation images were calculated with deformable image registration to map the end-expiratory and end-inspiratory CT

Corresponding Author: Tokihiro Yamamoto, 4501 X Street, G-145, Sacramento, CA 95817, Phone: (916) 734-0604, toyamamoto@ucdavis.edu.

Declarations of interest: None

images and quantitative analysis for regional volume changes as surrogates for ventilation. Perfusion images were calculated by subtracting the end-inspiratory precontrast CT from the deformably-registered end-inspiratory postcontrast CT, yielding a map of regional Hounsfield unit enhancement as a surrogate for perfusion. Ventilation-perfusion matching, spatial heterogeneity, and gravitationally directed gradients were compared between two groups using a Wilcoxon rank-sum test.

Results—The normal group had significantly higher Dice similarity coefficients for spatial overlap of segmented functional volumes between ventilation and perfusion (median 0.40 vs. 0.33, p=0.05), suggesting stronger ventilation-perfusion matching. The normal group also had greater Spearman's correlation coefficients based on 16 regions of interest (median 0.58 vs. 0.40, p=0.09). The coefficients of variation were comparable (median, ventilation 0.71 vs. 0.91, p=0.60; perfusion 0.63 vs. 0.75, p=0.27). The linear regression slopes of gravitationally directed gradient were also comparable for ventilation (median, ventilation −0.26 vs. −0.18, p=0.19; perfusion −0.17 vs. −0.06, p=0.11).

Conclusion—These findings provide proof-of-principle for single-energy CT ventilation/perfusion imaging.

Keywords

pulmonary functional imaging; ventilation; perfusion; single-energy computed tomography (CT); deformable image registration

1. Introduction

Pulmonary function tests (PFTs) are non-invasive and simple tests that provide important information about global lung function. Although PFTs are a well-established method to measure the global lung function, they do not provide spatial information about regional lung dysfunction (1). PFTs are not sensitive enough to detect early lung dysfunction (2), especially in the case of heterogeneous ventilation and perfusion abnormalities such as pulmonary embolism. Pulmonary embolism can be diagnosed with imaging techniques, such as ventilation and perfusion scintigraphy (or single-photon emission computed tomography (SPECT)) and CT angiography (3). Both imaging techniques have been found to have high diagnostic accuracy (4). However, combined assessment of regional ventilation and perfusion with SPECT has a higher sensitivity and specificity than CT angiography (5). Moreover, combined assessment of ventilation and perfusion has the potential to serve as a sensitive biomarker of early stage chronic obstructive pulmonary disease (COPD) (6, 7) and pulmonary hypertension (8). These findings suggest the importance of combined assessment of regional ventilation and perfusion in the evaluation of lung diseases.

Several imaging modalities can be used for combined assessment of pulmonary ventilation and perfusion. Planar scintigraphy and SPECT have been widely accepted as clinical standard imaging modalities for ventilation and perfusion assessment. More advanced imaging methods have also recently been investigated, including positron emission tomography (PET) (4), magnetic resonance imaging (MRI) (9), and dual-energy CT (10). Both ventilation and perfusion images can also be acquired with an emerging modality

based on single-energy CT and image processing/analysis (referred to as single-energy CT ventilation/perfusion imaging). Regional ventilation can be estimated based on the local volume change between inhalation and exhalation CT images (11, 12). Moreover, regional perfusion can be estimated based on regional HU enhancement in contrast-enhanced CT images (13, 14). Among these functional imaging methods, single-energy CT ventilation/perfusion imaging has great potential for widespread adoption, as single-energy CT scanners are available in most centers. Ventilation imaging does not require any tracers or contrast agents, while perfusion imaging only requires intravenous (IV) injection of iodinated contrast agents that are frequently used in clinical practice. Several studies have extensively investigated the accuracy and reproducibility of single-energy CT ventilation imaging in animal models (15–17) and human subjects (18–20), indicating its physiological significance. The feasibility of single-energy CT pulmonary perfusion imaging has also been demonstrated through animal studies (13, 14). However, to the best of our knowledge, no studies have been conducted on the combined assessment of ventilation and perfusion (*e.g.*, regional ventilation-perfusion matching) with single-energy CT.

The purpose of this study was to establish a proof-of-principle for single-energy CT ventilation/perfusion imaging. We compared ventilation-perfusion matching between normal and diseased lungs using two measures: (1) Spearman's correlation coefficient based on 16 regions of interest (ROIs) (defined by dividing the lungs), and (2) Dice similarity coefficients (DSCs) for the spatial overlap of segmented functional volumes. Moreover, we compared spatial heterogeneity and the gravitationally directed gradients of regional ventilation and perfusion between normal and diseased lungs.

2. Methods and materials

2.1. Subjects

We used a total of 17 canines (specifically, 8 canines with normal lungs and 9 canines with diseased lungs (including primary lung tumor, lung metastasis, and bronchointerstitial pneumonia)). The canines had to be at least one year old, weigh between 10 and 50 kg, and demonstrate adequate health and organ function as determined by physical examination, complete blood count, and a chemistry panel to verify that anesthesia could be safely administered. The experimental protocol was approved by the institutional clinical trials review board and the institutional animal care and use committee. Written informed consent was obtained from owners.

2.2. Overview of single-energy CT ventilation/perfusion imaging

Figure 1 shows a schematic diagram for single-energy CT ventilation/perfusion imaging and the studies performed. Three CT scans at end-expiration ($CT^{pre}_{end\_exp}$), mid-inspiration ($CT^{pre}_{mid\_ins}$), and end-inspiration ($CT^{pre}_{end\_ins}$) were obtained before IV injection of iodinated contrast for ventilation imaging, followed by another CT scan at end-inspiration after contrast injection ($CT^{post}_{end\_ins}$) for perfusion imaging. Deformable image registration (DIR) was used to spatially map the four CT image datasets. A ventilation image was calculated

with the deformably registered $CT^{pre}_{end\_exp}$ and $CT^{pre}_{end\_ins}$, and the HU-based metric (11) as a surrogate for regional ventilation. The DIR between $CT^{pre}_{end\_exp}$ and $CT^{pre}_{end\_ins}$ was performed through two steps: $CT^{pre}_{end\_exp}$(moving) to $CT^{pre}_{mid\_ins}$ (fixed) and $CT^{pre}_{mid\_ins}$ (moving) to $CT^{pre}_{end\_ins}$ (fixed), owing to large deformation. A perfusion image was created with the deformably registered $CT^{post}_{end\_ins}$ and $CT^{pre}_{end\_ins}$ by subtraction of the precontrast image dataset from the postcontrast image dataset, yielding a map of regional HU enhancement as a surrogate for regional perfusion.

2.3. Animal preparation and CT acquisition

All canines were maintained under general anesthesia for the duration of the imaging studies. The anesthesia was induced with Propofol (2 mg/kg IV) and midazolam (0.1 mg/kg IV) to effect in most cases. Heart rate, arterial pressure, body temperature, depth of anesthesia, and end-tidal carbon dioxide were monitored throughout the anesthetic procedure.

CT scans were performed with a LightSpeed 16-slice CT scanner (GE Healthcare, Waukesha, WI). The scan parameters were as follows: the tube voltage was 120 kV; the tube current was 150 mA; the rotation time was 1.0 s; and the pitch was 1.375. The images were reconstructed with 1.25-mm slice thickness using a sharp reconstruction kernel (GE Lung). Three CT scans at end-expiration, mid-inspiration, and end-inspiration were obtained before IV injection of iodinated contrast, followed by another CT scan at end-inspiration after contrast injection. All CT images were acquired in the prone position using a breath-hold technique. Assisted hyperventilation was performed before CT scans to facilitate breath-hold. An iodinated contrast material (3 mL/kg; Isovue, 370 mg of iodine/mL; Bracco Diagnostics, Cranbury Township, NJ) was injected into the cephalic vein at a flow rate of 4 mL/s. The postcontrast scan was initiated with a delay of 13 s to 20 s, depending on the volume of the contrast agent administered, which was adjusted according to body weight. The 13–20 s delay time is consistent with previous CT pulmonary perfusion studies based on breath-hold scans (13, 21). Fuld *et al.* (21) demonstrated a strong correlation between the iodine map of dual-energy CT based on a 15 s scan delay and pulmonary blood flow assessed with dynamic CT imaging.

2.4. Deformable image registration (DIR)

For the ventilation image calculation, DIR was used to spatially map the $CT^{pre}_{end\_exp}$ and $CT^{pre}_{end\_ins}$ images. Two separate registrations ($CT^{pre}_{end\_exp}$(moving) to $CT^{pre}_{mid\_ins}$ (fixed), and $CT^{pre}_{mid\_ins}$ (moving) to $CT^{pre}_{end\_ins}$ (fixed)) were performed to improve the spatial registration accuracy of the DIR between the maximum phases. For the perfusion image calculation, the DIR was used to spatially map the $CT^{post}_{end\_ins}$ (moving) and $CT^{pre}_{end\_ins}$ (fixed) images. The DIRs were performed using elastix, an open source software package (22). The DIR parameter settings were similar to Yamamoto *et al.* (14), which was based on the optimized settings for thoracic CT images established by (23). The DIR was performed in a multigrid

setting that was driven by a similarity function and a transform bending energy penalty (24) (set to 0.05 for all conditions). Two similarity functions—namely, mutual information (MI) and normalized cross correlation (NCC)—were compared to select the function that showed better performance based on visual and quantitative assessment. For the image data, Gaussian pyramids were used for down-sampling to increase robustness. A multigrid approach was used for the B-spline transformation. The DIR was performed with lung masks that were generated by segmenting the lungs on both the fixed and moving CT images and merging those segmented lungs together.

The accuracy of the DIR was quantitatively evaluated based on the target registration error (TRE) of anatomic pulmonary landmarks and the singularity of the deformation field. We used the iX software (25) to generate 50 landmarks per subject distributed throughout the lungs. Manual annotation of these landmarks was performed by a medical physicist. The Jacobian determinant of the displacement vector field (DVF) was calculated for each voxel and analyzed to examine whether there was any voxel with a negative Jacobian value. The negative Jacobian was a singularity in the deformation. The TRE was evaluated for the following two DIR scenarios: $CT^{pre}_{end\_exp}$(moving) to $CT^{pre}_{mid\_ins}$ (fixed), and $CT^{post}_{end\_ins}$ (moving) to $CT^{pre}_{end\_ins}$ (fixed). The TRE for DIR between $CT^{pre}_{mid\_ins}$ to $CT^{pre}_{end\_ins}$ was not evalauted because the lung volume change between $CT^{pre}_{mid\_ins}$ and $CT^{pre}_{end\_ins}$ was considerably smaller than between $CT^{pre}_{end\_exp}$ and $CT^{pre}_{mid\_ins}$ (the mean percentage lung volume change, 110% vs. 134%), and hence the accuracy of DIR between $CT^{pre}_{mid\_ins}$ and $CT^{pre}_{end\_ins}$ was assumed to be no worse than DIR between $CT^{pre}_{end\_exp}$ and $CT^{pre}_{mid\_ins}$.

2.5. CT ventilation imaging

Ventilation images were calculated with the deformably registered $CT^{pre}_{end\_exp}$ and $CT^{pre}_{end\_ins}$ images. Regional ventilation was quantified using the HU-based metric (V^{HU}) (11), which was defined based on the relationship between the local HU change and the local volume change. The V^{HU} in the voxel at location x is given as follows:

$$V^{\mathrm{HU}} = \frac{HU^{\mathrm{pre}}_{\mathrm{end\_exp}}(x+u) - HU^{\mathrm{pre}}_{\mathrm{end\_ins}}(x)}{HU^{\mathrm{pre}}_{\mathrm{end\_ins}}(x) + 1000}\rho_{\mathrm{scaling}}, \quad (1)$$

where HU is the HU value; u is the displacement vector mapping the voxel of the end-expiratory image to the corresponding location of the end-inspiratory image; and ρ_{scaling} is the CT density scaling factor, which takes a value ranging from zero for the voxel with the lowest CT density to one for the voxel with the highest CT density (−250 HU) (18, 20). We applied a mass correction to $HU_{\mathrm{end\_ins}}$ to account for the changes in the blood distribution between the end-expiratory and end-inspiratory images, in the same manner as that in (12). The influence of CT noise was reduced by smoothing the CT images after DIR using a 3D Gaussian filter kernel with a variance σ = 1.5 mm before computing V^{HU}. The smoothing level was applied to allow removal of abnormal high-intensity tails of ventilation and perfusion values and small changes from the original distributions. All CT images were

smoothed in the same manner for both ventilation and perfusion quantification. Abnormally high ventilation values were observed in peripheral lung regions (Supplementary Fig A.1(a)), which was likely due to image smoothing and DIR errors. Thus, we excluded voxels within 1.5 mm of the outer boundaries of lung masks from the analysis (Supplementary Fig A.1(b)).

For the analysis, normalization is necessary to compare ventilation and perfusion, which are measured using different scales. The ventilation values were normalized by the mean of the highest 5% of the ventilation values, yielding a ventilation distribution with a range of approximately 0 to 1. This normalization method is consistent with that implemented in the ^{129}Xe MRI ventilation study reported by (26). Given that abnormal ventilation values may be caused by image processing, abnormally high and low ventilation values (mean ± 2SD as a threshold) were excluded from the analysis.

2.6. CT pulmonary perfusion imaging

Perfusion images were calculated by subtracting the $CT^{pre}_{end\_ins}$ from the deformably registered $CT^{post}_{end\_ins}$, yielding a map of the regional HU enhancement as a surrogate for perfusion (Q) (14). Q in the voxel at location x, is given as follows:

$$Q = HU^{post}_{end\_ins}(x+u) - {}^{corrected}HU^{pre}_{end\_ins}(x), \quad (2)$$

where HU^{post} and HU^{pre} are the HU values of the $CT^{post}_{end\_ins}$ and $CT^{pre}_{end\_ins}$ images, respectively; and u is the displacement vector mapping the voxel of the $CT^{post}_{end\_ins}$ image to the corresponding location of the $CT^{pre}_{end\_ins}$ image. Given that the HU values of the lung tissues varied with the lung inflation level, we corrected the HUs of $CT^{pre}_{end\_ins}$ for the lung inflation variation based on a relationship between the HU for each voxel and the total lung volume as a measure of the lung inflation level (yielding $^{corrected}HU$). This correction is consistent with that implemented in (14). The CT images were also smoothed using a 3D Gaussian filter kernel with a variance σ = 1.5 mm before computing Q. The perfusion image was also normalized by dividing the mean of the highest 5% of the perfusion values. Given that abnormal perfusion values may be caused by image processing and CT artifacts (*i.e.*, streak artifacts), abnormally high and low perfusion values (mean ± 2SD as a threshold) were excluded from the analysis.

2.7. Analysis of the ventilation and perfusion images

Ventilation-perfusion matching was quantified using two measures: (1) the Spearman's correlation coefficient based on 16 ROIs (defined by dividing the lungs), and (2) DSCs for the spatial overlap of four segmented functional volumes (defect, and low-, moderate-, and high-functional volumes). Efficient gas exchange requires intimate matching of regional ventilation and perfusion, *i.e.*, an ideal ventilation-perfusion ratio of 1.0. Gas exchange impairment occurs when ventilation and perfusion are mismatched. We generated lung masks by delineating lung voxels with HU values less than a threshold of −250 HU (12)

within the lung contours generated by the model-based segmentation. To quantify Spearman's correlation coefficients, each of the right and left lungs were equally divided into 8 ROIs (AP × RL × SI: 2 × 2 × 2 regions). The mean normalized ventilation and perfusion values were then calculated for each ROI, and used to quantify the correlation. To quantify DSCs for the spatial overlap of segmented functional volumes, we performed hierarchical k-means clustering (27) to partition the ventilation and perfusion images into four functional volumes in a manner similar to a previously described method for ^{3}He MRI ventilation images (28). Figure 2 shows a schematic of the hierarchical k-means clustering method, which mainly consists of seven steps: (1) the function image was initially divided into left and right lung, (2) k-means with 10 clusters was applied to the two volumes, (3) the top five clusters from step 2 were merged to represent higher functional region and the residual five volumes were also merged to represent lower functional region, (4) k-means with 10 clusters were then reapplied to the higher and lower functional region, (5) the clusters were merged to higher and lower functional region as with step 3, (6) the segmented volumes were sorted by the mean of the ventilation or perfusion values in each ROI, (7) the sorted volumes were merged every two ROIs into a single ROI from the lowest to the highest functional volume. For both steps 2 and 4, the initial centroids were determined by dividing each distribution into 10 deciles, the upper limits of which are defined by the 10th, 20th, …, 90th, and 100th percentile, and selecting the interval center as the centroid for each cluster. The resulting four segmented functional volumes of ventilation were compared with those of perfusion to quantify DSCs. For the k-means clustering, the optimal number of clusters (step 2 above) in a data set is a fundamental issue in partitioning clusters. The optimal number of clusters was determined based on minimizing sum of squared distances within a cluster. We measured the sum of squared distances by varying cluster number from 4 to 20, and the optimal number of clusters was 10 in our study.

Spatial heterogeneity was quantified based on the coefficient of variation (CoV). The CoV was calculated from mean and standard deviation of normalized ventilation and perfusion distribution, divided the standard deviation by the mean.

The gravitationally directed gradient was quantified based on the linear regression slope for the relationship between the ventral-to-dorsal distance and normalized ventilation or perfusion values. The total lung was divided into five coronally sectioned ROIs, equally spaced along the ventral-to-dorsal direction. The mean normalized ventilation and perfusion values were calculated for each ROI.

We compared ventilation-perfusion matching (the Spearman's correlation coefficients were converted into z sores using Fisher's transformation), spatial heterogeneity, and gravitationally directed gradients between the normal and diseased lung groups using a Wilcoxon rank-sum test.

3. Results

3.1. DIR accuracy

MI resulted in smaller TRE for DIR between $CT^{pre}_{end\_exp}$ and $CT^{pre}_{mid\_ins}$ (NCC: 1.4 ± 2.0 mm, MI: 0.87 ± 1.0 mm), and TRE for DIR between $CT^{pre}_{end\_ins}$ and $CT^{post}_{end\_ins}$ differed only slightly (NCC: 0.57 ± 0.55 mm, MI: 0.64 ± 0.54 mm). Negative Jacobians were observed only in DIR based on MI between $CT^{pre}_{end\_ins}$ and $CT^{post}_{end\_ins}$ (mean 0.03 ± 0.07 %, range 0.0–0.3 %). Examination of the other registrations confirmed that all Jacobian values had positive values. Consequently, MI was selected for the DIR between $CT^{pre}_{end\_exp}$ and $CT^{pre}_{mid\_ins}$ and between $CT^{pre}_{mid\_ins}$ and $CT^{pre}_{end\_ins}$, and NCC was selected for the DIR between $CT^{post}_{end\_ins}$ and $CT^{pre}_{end\_ins}$. Across the entire dataset, the mean TREs were smaller than the one-voxel size of 0.6 × 0.6 × 1.25 mm^3, while the registration errors ranged up to 10 mm. The large registration errors were observed for the features located in diaphragm region and near streak artifacts in postcontrast CT.

The DIR accuracy was comparable between the diseased group and the normal group in those DIR scenarios. The TRE for DIR between $CT^{pre}_{end\_exp}$ and $CT^{pre}_{mid\_ins}$ was smaller than the one-voxel size (median, the diseased lung group 0.67 mm; the normal lung group 1.1 mm). The TRE for DIR between $CT^{post}_{end\_ins}$ and $CT^{pre}_{end\_ins}$ was also smaller than the one-voxel size (median, the diseased lung group 0.47 mm; the normal lung group 0.56 mm). Moreover, there were no significant differences in visual assessment of the DIR accuracy between the two group.

3.2. Ventilation-perfusion matching

Figure 3 shows scatter plots of normalized ventilation and perfusion, and example images of ventilation and perfusion for the four representative subjects: normal lung subjects with the strongest correlation (subject N1: Spearman's correlation coefficient R = 0.78 and mean DSC = 0.40) and a weak correlation (subject N2: R = 0.39, mean DSC = 0.33) between ventilation and perfusion, and diseased lung subjects with a strong correlation (subject D1: R = 0.64, mean DSC = 0.45) and the lowest correlation (subject D2: R = −0.03, mean DSC = 0.33) between ventilation and perfusion.

Figure 4 shows a comparison of the Spearman's correlation coefficients between regional ventilation and perfusion for the normal lung group and those for the diseased lung group. The median Spearman's correlation coefficients between ventilation and perfusion were 0.58 (range 0.39–0.92) for the normal lung subjects and 0.40 (range −0.03–0.69) for the diseased lung subjects. The correlation coefficients of normal lung individuals were distributed in a close cluster around the median of the box plot, whereas those of diseased lung subjects were distributed over a wider range with higher standard deviation. The difference between the two groups were not statistically significant at the 0.05 level (p=0.09).

Figure 5 shows a comparison of the DSCs for the spatial overlap of segmented functional volumes between ventilation and perfusion for the normal lung group and those for the

diseased lung group. The mean DSCs of four segmented functional volumes were significantly higher in the normal subjects than in the diseased subjects (median 0.40 vs. 0.33, p=0.05). The DSCs for the each volumes (lung defects, and low-, moderate- and high-functional volumes) were higher in the normal lung subjects than in the diseased lung subjects (median, defects 0.39 vs. 0.32; low 0.41 vs. 0.28; moderate 0.25 vs. 0.21; high 0.46 vs. 0.34). The differences in DSC score for these volumes were not statistically significant at the 0.05 level (defects p=0.27; low p=0.08; moderate p=0.48; high p=0.19). These results indicate a stronger ventilation-perfusion matching for the normal lung subjects than the diseased lung subjects.

3.4. Spatial heterogeneity

Figure 6 shows a comparison of CoVs of regional ventilation and perfusion for the normal lung group and those for the diseased lung group. The median CoVs for the normal lung subjects were 0.71 for ventilation and 0.63 for perfusion, which were not significantly different from those for the diseased lung subjects (0.91 for ventilation, p=0.60; 0.75 for perfusion, p=0.27).

3.5. Gravitationally directed gradients

Gravitationally directed gradients of ventilation and perfusion were observed for both groups, indicating higher ventilation or perfusion in the ventral regions than in the dorsal regions. Figure 7 shows examples gradients of ventilation and perfusion for subjects N1 and D2. Figure 8 shows a comparison of the linear regression slopes of ventilation and perfusion for the normal lung group and those for the diseased lung group. Both ventilation and perfusion gradients tended to be steeper in the normal lung group than in the diseased lung group (median −0.26 vs. −0.18 for ventilation; −0.17 vs. −0.06 for perfusion). However, the differences were not statistically significant (p=0.19 for ventilation; p=0.11 for perfusion).

4. DISCUSSION

This is the first study to investigate the combined assessment of ventilation and perfusion with single-energy CT ventilation/perfusion imaging. We demonstrated stronger ventilation-perfusion matching (*i.e.*, significantly greater DSCs and nearly significantly greater Spearman's correlation coefficients) in the normal lung subjects than in the diseased lung subjects, which is consistent with previous studies (7, 29, 30), providing a proof-of-principle for single-energy CT ventilation/perfusion imaging. Table 1 shows a summary of previous animal and human studies on ventilation-perfusion matching (7, 29–37). We observed only moderate DSCs and Spearman's correlation coefficients in most normal lung subjects, which might reflect limitations of the current method for single-energy CT ventilation/perfusion imaging. Another possible explanation is that anesthesia used for all subjects may have led to increased ventilation-perfusion mismatch (38).

We observed a non-significant difference in the CoV between the normal and diseased groups. Previous studies have shown inconsistent findings including both significant and non-significant differences in the CoV between the normal and diseased subjects (30, 39) (see Table 1). To identify potential confounders that might affect the CoV, we investigated

several factors related to CT imaging and compared those between the normal and diseased groups. For CT ventilation, the lung volume change between two paired CT scans was found to be moderately correlated with the CoV (R = −0.66) (Supplementary Fig B.2), suggesting that a small volume change might lead to a large CoV perhaps because of a relatively low signal-to-noise ratio or small HU change. An outlier normal subject with a large CoV of 2.40 (see Fig 6) showed a considerably smaller lung volume change between $CT^{pre}_{end\_exp}$ and $CT^{pre}_{end\_ins}$ (129%) compared to the other normal subjects (mean 153±14%). However, there was no significant difference in the lung volume change between the normal and diseased groups (153±14% vs. 144±11%, p=0.23). For CT perfusion, the volume of negative HU enhancement was found to be strongly correlated with the CoV (R = 0.96) (Supplementary Fig C.3), most likely because negative HU enhancement caused by streak artifacts leads to large standard deviations (14). Although most of abnormal CT perfusion values by severe streak artifacts could be suppressed by a thresholding based filtering, the negative HU enhancements by mild CT artifacts still remained on the perfusion maps. Future studies with strategies that reduce these CT artifacts would provide insights into the accuracy of CT ventilation/perfusion imaging.

We observed a non-significant difference in the gravitationally directed gradients for ventilation between the normal and diseased groups. The gravitationally directed gradients were studied to examine whether ventilation and perfusion imaging can demonstrate the known effect of gravity (*i.e.,* greater ventilation and perfusion in gravity-dependent regions than in nondependent regions) under normal conditions as shown in several studies (30, 40, 41) (see Table 1). The presented results were only for the lung cancer and interstitial pneumonia patients, and not including any COPD patients. The various pathologies in the diseased group is a potential reason for the non-significant difference in the gravitationally directed gradients between the two groups.

The present study has several limitations. First, as described above, our study used canines with various types of lung diseases, and some of those may not be an ideal disease model of heterogeneous ventilation and perfusion abnormalities. For example, canines with small lung tumors might have little effect on regional ventilation and perfusion, which may have also contributed to the non-significant differences in the median CoVs of ventilation and perfusion and the gravitationally directed gradient of ventilation between the two groups. Models with a higher heterogeneity of ventilation and perfusion, such as advanced COPD, will be considered in future studies. Another limitation to consider is DIR registration errors. The majority of TREs were smaller than the voxel dimension; however, TREs ranged up to 10 mm. The results of the EMPIRE10 challenge also exhibited larger registration errors for the breath-hold CT images because of a large deformation (42). Given that DIR errors directly affect the accuracy of ventilation calculations, future developments of DIR algorithms that can better handle large deformations would improve CT ventilation imaging. Finally, the statistical power of this study was limited due to a small sample size. Further studies with a larger sample size are required to confirm the findings from this study.

Further work remains to be performed to investigate the accuracy and precision of single-energy CT ventilation/perfusion imaging. Previous studies have assessed the accuracy (15–

20) and reproducibility (43, 44) of single-energy CT ventilation imaging, whereas there is no study that quantifies those of single-energy CT perfusion imaging. More studies such as cross-modalities comparisons and reproducibility of CT pulmonary perfusion images between the two time points are needed in future work. In addition, further study to quantify the repeatability of the technique for quantitative assessment of combined ventilation and perfusion, e.g., test-retest reliability method, is required in order to understand the source of variability in spatial correlation.

Single-energy CT ventilation/perfusion (V/Q) imaging has great potential for widespread adoption, as single-energy CT scanners are available in most centers. Furthermore, ventilation imaging does not require any tracers or contrast agents, and perfusion imaging only requires iodinated contrast agents that is widely used in routine clinical practice. Compared to conventional V/Q imaging approaches (including scintigraphy planar imaging and SPECT), single-energy CT V/Q imaging can provide a higher spatial and temporal resolution, and thereby allows more accurate quantification of regional lung function.

5. Conclusion

This canine study demonstrated significantly better regional ventilation-perfusion matching for the normal lung subjects than the diseased lung subjects, providing a proof-of-principle for single-energy CT ventilation/perfusion imaging. Further studies such as cross-modality image comparisons are needed for validation.

Supplementary Material

Refer to Web version on PubMed Central for supplementary material.

Acknowledgments

This study was supported by Philips Healthcare/Radiological Society of North America (RSNA) Research Seed Grant No. RSD1458. The authors are grateful to Teri Guerrero of the Department of Surgical and Radiological Sciences at the University of California Davis School of Veterinary Medicine for her support in coordinating the canine clinical trial. The authors also thank the veterinary radiology staff for their clinical support.

Abbreviations

COPD	chronic obstructive pulmonary disease
CoV	coefficient of variation
CT	computed tomography
DIR	deformable image registration
DSC	dice similarity coefficient
HU	Hounsfield unit
MI	mutual information
MRI	magnetic resonance imaging

NCC	normalized cross correlation
PET	positron emission tomography
PFT	pulmonary function test
ROI	region of interest
SPECT	single-photon emission computed tomography
TRE	target registration error

References

1. Han MK, Agusti A, Calverley PM, et al. Chronic obstructive pulmonary disease phenotypes: the future of COPD. American journal of respiratory and critical care medicine. 2010; 182(5):598–604. [PubMed: 20522794]
2. Taplin GV, Tashkin DP, Chopra SK, et al. Early detection of chronic obstructive pulmonary disease using radionuclide lung-imaging procedures. Chest. 1977; 71(5):567–75. [PubMed: 856554]
3. Bajc M, Jonson B. Ventilation/Perfusion SPECT for Diagnosis of Pulmonary Embolism and Other Diseases. International journal of molecular imaging. 2011; 2011:682949. [PubMed: 21490731]
4. Hofman MS, Beauregard JM, Barber TW, Neels OC, Eu P, Hicks RJ. 68Ga PET/CT ventilation-perfusion imaging for pulmonary embolism: a pilot study with comparison to conventional scintigraphy. J Nucl Med. 2011; 52(10):1513–9. [PubMed: 21908388]
5. Gutte H, Mortensen J, Jensen CV, et al. Detection of pulmonary embolism with combined ventilation-perfusion SPECT and low-dose CT: head-to-head comparison with multidetector CT angiography. J Nucl Med. 2009; 50(12):1987–92. [PubMed: 19910421]
6. Jogi J, Ekberg M, Jonson B, Bozovic G, Bajc M. Ventilation/perfusion SPECT in chronic obstructive pulmonary disease: an evaluation by reference to symptoms, spirometric lung function and emphysema, as assessed with HRCT. European journal of nuclear medicine and molecular imaging. 2011; 38(7):1344–52. [PubMed: 21365251]
7. Suga K, Kawakami Y, Koike H, et al. Lung ventilation-perfusion imbalance in pulmonary emphysema: assessment with automated V/Q quotient SPECT. Annals of nuclear medicine. 2010; 24(4):269–77. [PubMed: 20340054]
8. Tunariu N, Gibbs SJ, Win Z, et al. Ventilation-perfusion scintigraphy is more sensitive than multidetector CTPA in detecting chronic thromboembolic pulmonary disease as a treatable cause of pulmonary hypertension. J Nucl Med. 2007; 48(5):680–4. [PubMed: 17475953]
9. Togao O, Ohno Y, Dimitrov I, Hsia CC, Takahashi M. Ventilation/perfusion imaging of the lung using ultra-short echo time (UTE) MRI in an animal model of pulmonary embolism. Journal of magnetic resonance imaging : JMRI. 2011; 34(3):539–46. [PubMed: 21761465]
10. Thieme SF, Johnson TR, Reiser MF, Nikolaou K. Dual-energy lung perfusion computed tomography: a novel pulmonary functional imaging method. Seminars in ultrasound, CT, and MR. 2010; 31(4):301–8.
11. Guerrero T, Sanders K, Noyola-Martinez J, et al. Quantification of regional ventilation from treatment planning CT. Int J Radiat Oncol Biol Phys. 2005; 62(3):630–4. [PubMed: 15936537]
12. Guerrero T, Sanders K, Castillo E, et al. Dynamic ventilation imaging from four-dimensional computed tomography. Phys Med Biol. 2006; 51(4):777–91. [PubMed: 16467578]
13. Wildberger JE, Klotz E, Ditt H, Spuntrup E, Mahnken AH, Gunther RW. Multislice computed tomography perfusion imaging for visualization of acute pulmonary embolism: animal experience. European radiology. 2005; 15(7):1378–86. [PubMed: 15776240]
14. Yamamoto T, Kent MS, Wisner ER, et al. Single-energy computed tomography-based pulmonary perfusion imaging: Proof-of-principle in a canine model. Med Phys. 2016; 43(7):3998–4007. [PubMed: 27370118]

15. Reinhardt JM, Ding K, Cao K, Christensen GE, Hoffman EA, Bodas SV. Registration-based estimates of local lung tissue expansion compared to xenon CT measures of specific ventilation. Med Image Anal. 2008; 12(6):752–63. [PubMed: 18501665]
16. Fuld MK, Easley RB, Saba OI, et al. CT-measured regional specific volume change reflects regional ventilation in supine sheep. J Appl Physiol (1985). 2008; 104(4):1177–84. [PubMed: 18258804]
17. Ding K, Cao K, Fuld MK, et al. Comparison of image registration based measures of regional lung ventilation from dynamic spiral CT with Xe-CT. Med Phys. 2012; 39(8):5084–98. [PubMed: 22894434]
18. Yamamoto T, Kabus S, Lorenz C, et al. Pulmonary ventilation imaging based on 4-dimensional computed tomography: comparison with pulmonary function tests and SPECT ventilation images. Int J Radiat Oncol Biol Phys. 2014; 90(2):414–22. [PubMed: 25104070]
19. Vinogradskiy Y, Koo PJ, Castillo R, et al. Comparison of 4-dimensional computed tomography ventilation with nuclear medicine ventilation-perfusion imaging: a clinical validation study. Int J Radiat Oncol Biol Phys. 2014; 89(1):199–205. [PubMed: 24725702]
20. Kipritidis J, Siva S, Hofman MS, Callahan J, Hicks RJ, Keall PJ. Validating and improving CT ventilation imaging by correlating with ventilation 4D-PET/CT using 68Ga-labeled nanoparticles. Med Phys. 2014; 41(1):011910. [PubMed: 24387518]
21. Fuld MK, Halaweish AF, Haynes SE, Divekar AA, Guo J, Hoffman EA. Pulmonary perfused blood volume with dual-energy CT as surrogate for pulmonary perfusion assessed with dynamic multidetector CT. Radiology. 2013; 267(3):747–56. [PubMed: 23192773]
22. Klein S, Staring M, Murphy K, Viergever MA, Pluim JP. elastix: a toolbox for intensity-based medical image registration. IEEE Trans Med Imaging. 2010; 29(1):196–205. [PubMed: 19923044]
23. Metz CT, Klein S, Schaap M, van Walsum T, Niessen WJ. Nonrigid registration of dynamic medical imaging data using nD + t B-splines and a groupwise optimization approach. Med Image Anal. 2011; 15(2):238–49. [PubMed: 21075672]
24. Rueckert D, Sonoda LI, Hayes C, Hill DL, Leach MO, Hawkes DJ. Nonrigid registration using free-form deformations: application to breast MR images. IEEE Trans Med Imaging. 1999; 18(8):712–21. [PubMed: 10534053]
25. Murphy K, van Ginneken B, Klein S, et al. Semi-automatic construction of reference standards for evaluation of image registration. Med Image Anal. 2011; 15(1):71–84. [PubMed: 20709592]
26. Virgincar RS, Cleveland ZI, Kaushik SS, et al. Quantitative analysis of hyperpolarized (129)Xe ventilation imaging in healthy volunteers and subjects with chronic obstructive pulmonary disease. NMR in Biomedicine. 2013; 26(4):424–35. [PubMed: 23065808]
27. Lloyd SP. Least squares quantization in PCM. IEEE Transactions on Information Theory. 1982; 28(2):129–37.
28. Kirby M, Heydarian M, Svenningsen S, et al. Hyperpolarized 3He magnetic resonance functional imaging semiautomated segmentation. Acad Radiol. 2012; 19(2):141–52. [PubMed: 22104288]
29. Sando Y, Inoue T, Nagai R, Endo K. Ventilation/perfusion ratios and simultaneous dual-radionuclide single-photon emission tomography with krypton-81m and technetium-99m macroaggregated albumin. European journal of nuclear medicine. 1997; 24(10):1237–44. [PubMed: 9323264]
30. Vidal Melo MF, Winkler T, Harris RS, Musch G, Greene RE, Venegas JG. Spatial heterogeneity of lung perfusion assessed with (13)N PET as a vascular biomarker in chronic obstructive pulmonary disease. J Nucl Med. 2010; 51(1):57–65. [PubMed: 20008987]
31. Robertson HT, Glenny RW, Stanford D, McInnes LM, Luchtel DL, Covert D. High-resolution maps of regional ventilation utilizing inhaled fluorescent microspheres. J Appl Physiol (1985). 1997; 82(3):943–53. [PubMed: 9074986]
32. Altemeier WA, Robertson HT, McKinney S, Glenny RW. Pulmonary embolization causes hypoxemia by redistributing regional blood flow without changing ventilation. J Appl Physiol (1985). 1998; 85(6):2337–43. [PubMed: 9843561]
33. Altemeier WA, McKinney S, Glenny RW. Fractal nature of regional ventilation distribution. J Appl Physiol (1985). 2000; 88(5):1551–7. [PubMed: 10797111]

34. Melsom MN, Kramer-Johansen J, Flatebo T, Muller C, Nicolaysen G. Distribution of pulmonary ventilation and perfusion measured simultaneously in awake goats. Acta physiologica Scandinavica. 1997; 159(3):199–208. [PubMed: 9079150]

35. Yuan ST, Frey KA, Gross MD, et al. Semiquantification and classification of local pulmonary function by V/Q single photon emission computed tomography in patients with non-small cell lung cancer: potential indication for radiotherapy planning. J Thorac Oncol. 2011; 6(1):71–8. [PubMed: 21119546]

36. Ogawa Y, Ashizawa K, Hashmi R, Takemoto Y, Hayashi K. Regional ventilation-perfusion mismatch in interstitial pneumonia. Correlation between scintigraphy and CT. Clinical nuclear medicine. 1997; 22(3):166–71. [PubMed: 9067670]

37. Hwang HJ, Seo JB, Lee SM, et al. Assessment of Regional Xenon Ventilation, Perfusion, and Ventilation-Perfusion Mismatch Using Dual-Energy Computed Tomography in Chronic Obstructive Pulmonary Disease Patients. Investigative radiology. 2016; 51(5):306–15. [PubMed: 26685105]

38. Nyren S, Radell P, Mure M, et al. Inhalation anesthesia increases V/Q regional heterogeneity during spontaneous breathing in healthy subjects. Anesthesiology. 2010; 113(6):1370–5. [PubMed: 21068662]

39. Tzeng YS, Lutchen K, Albert M. The difference in ventilation heterogeneity between asthmatic and healthy subjects quantified using hyperpolarized 3He MRI. J Appl Physiol (1985). 2009; 106(3):813–22. [PubMed: 19023025]

40. Petersson J, Sanchez-Crespo A, Larsson SA, Mure M. Physiological imaging of the lung: single-photon-emission computed tomography (SPECT). J Appl Physiol (1985). 2007; 102(1):468–76. [PubMed: 16990505]

41. Bauman G, Lutzen U, Ullrich M, et al. Pulmonary functional imaging: qualitative comparison of Fourier decomposition MR imaging with SPECT/CT in porcine lung. Radiology. 2011; 260(2):551–9. [PubMed: 21586678]

42. Murphy K, van Ginneken B, Reinhardt JM, et al. Evaluation of registration methods on thoracic CT: the EMPIRE10 challenge. IEEE Trans Med Imaging. 2011; 30(11):1901–20. [PubMed: 21632295]

43. Du K, Bayouth JE, Cao K, Christensen GE, Ding K, Reinhardt JM. Reproducibility of registration-based measures of lung tissue expansion. Med Phys. 2012; 39(3):1595–608. [PubMed: 22380392]

44. Yamamoto T, Kabus S, von Berg J, et al. Reproducibility of four-dimensional computed tomography-based lung ventilation imaging. Acad Radiol. 2012; 19(12):1554–65. [PubMed: 22975070]

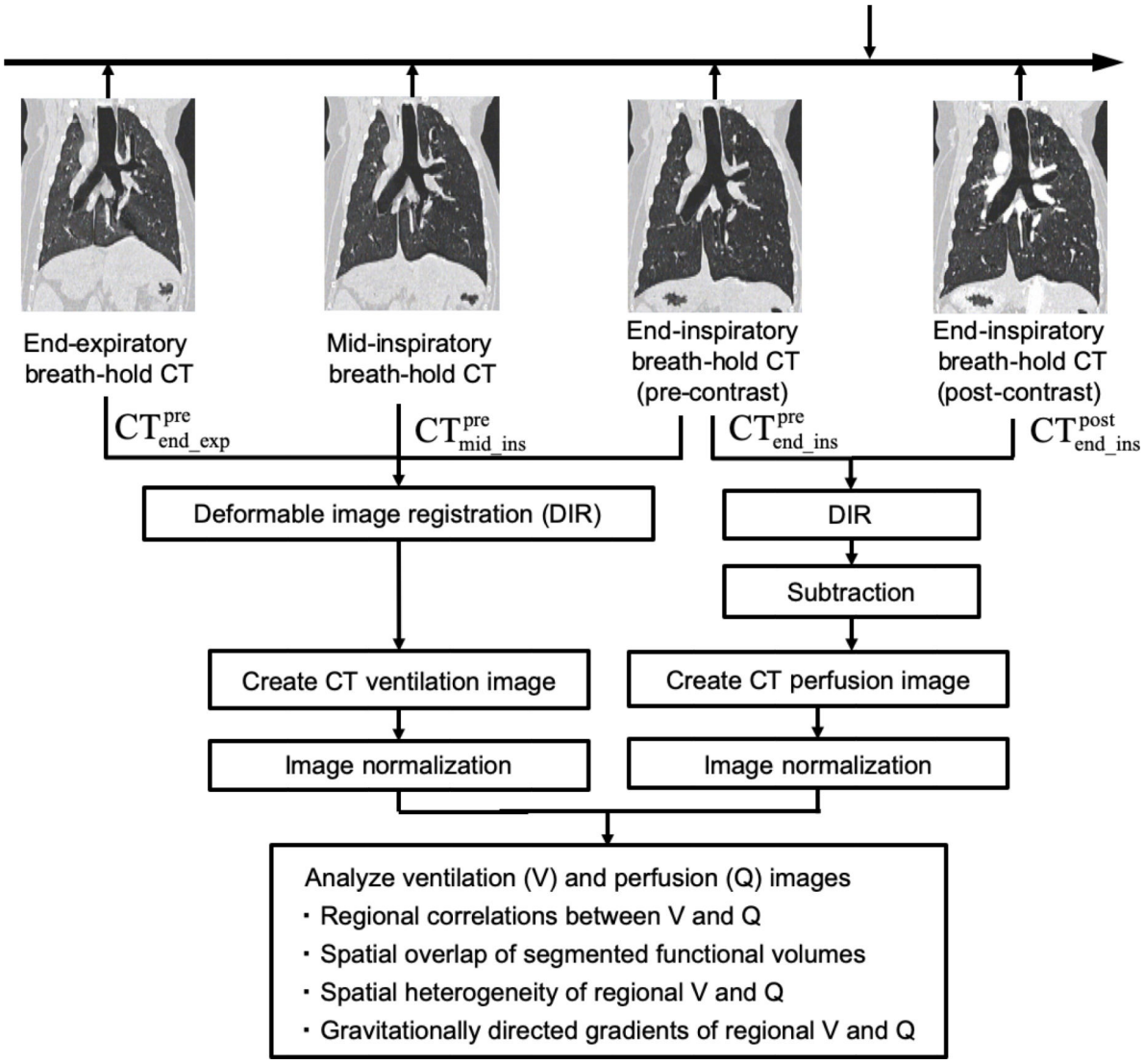

Fig 1.

Schematic of image acquisition, processing, and analysis for single-energy CT ventilation/perfusion imaging as well as the studies performed. Ventilation images were calculated with the deformably registered end-expiratory and end-inspiratory CT images. DIR was performed through two steps (end-expiration to mid-inspiration, and mid-inspiration to end-inspiration). Perfusion images were created by subtraction of the deformably registered precontrast image dataset from the postcontrast image dataset.

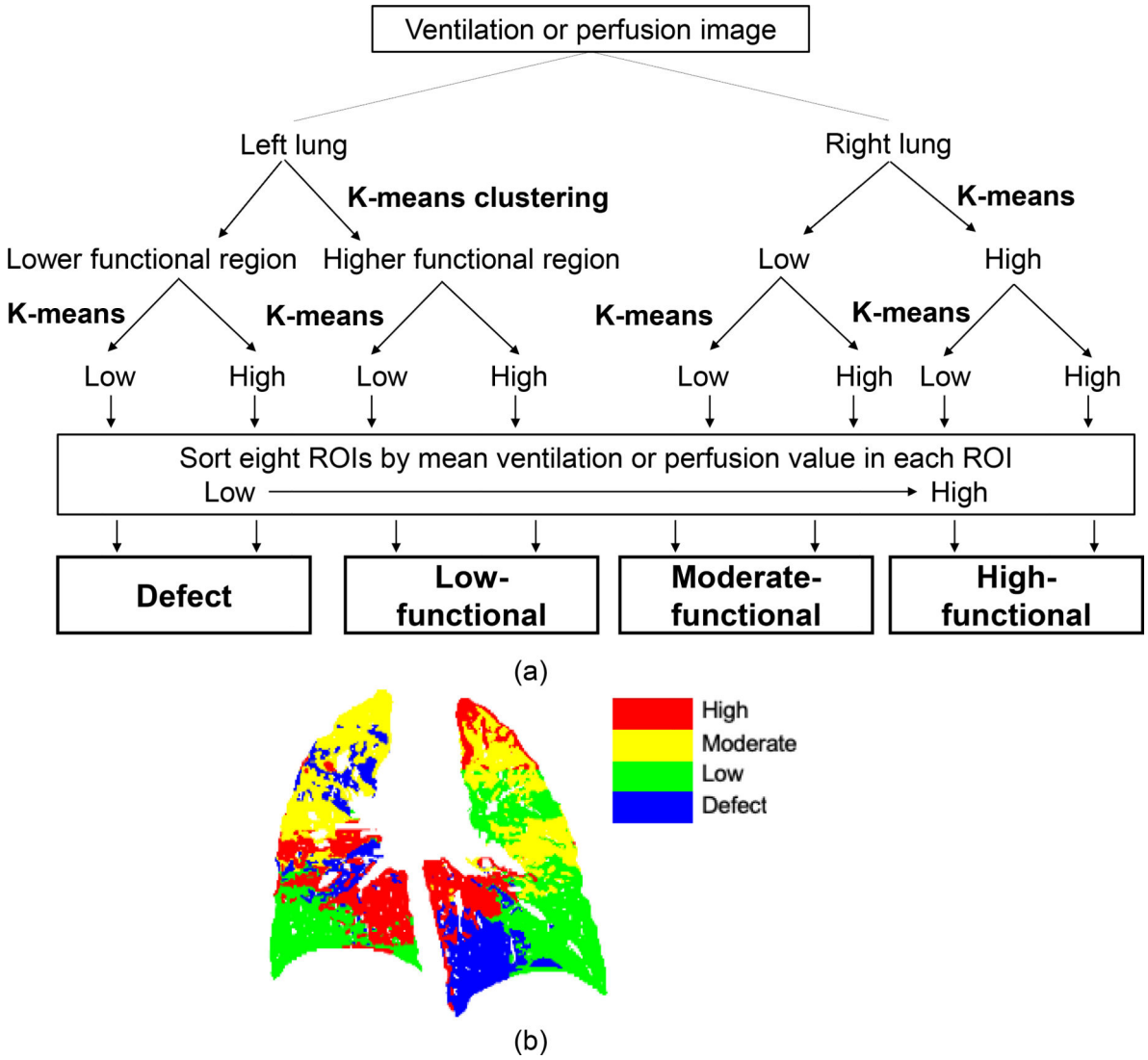

Fig 2.

(a) Schematic of hierarchical k-means clustering to segment four functional volumes (defect, and low-, moderate-, and high-functional volumes). (b) An example image of the four segmented functional volumes.

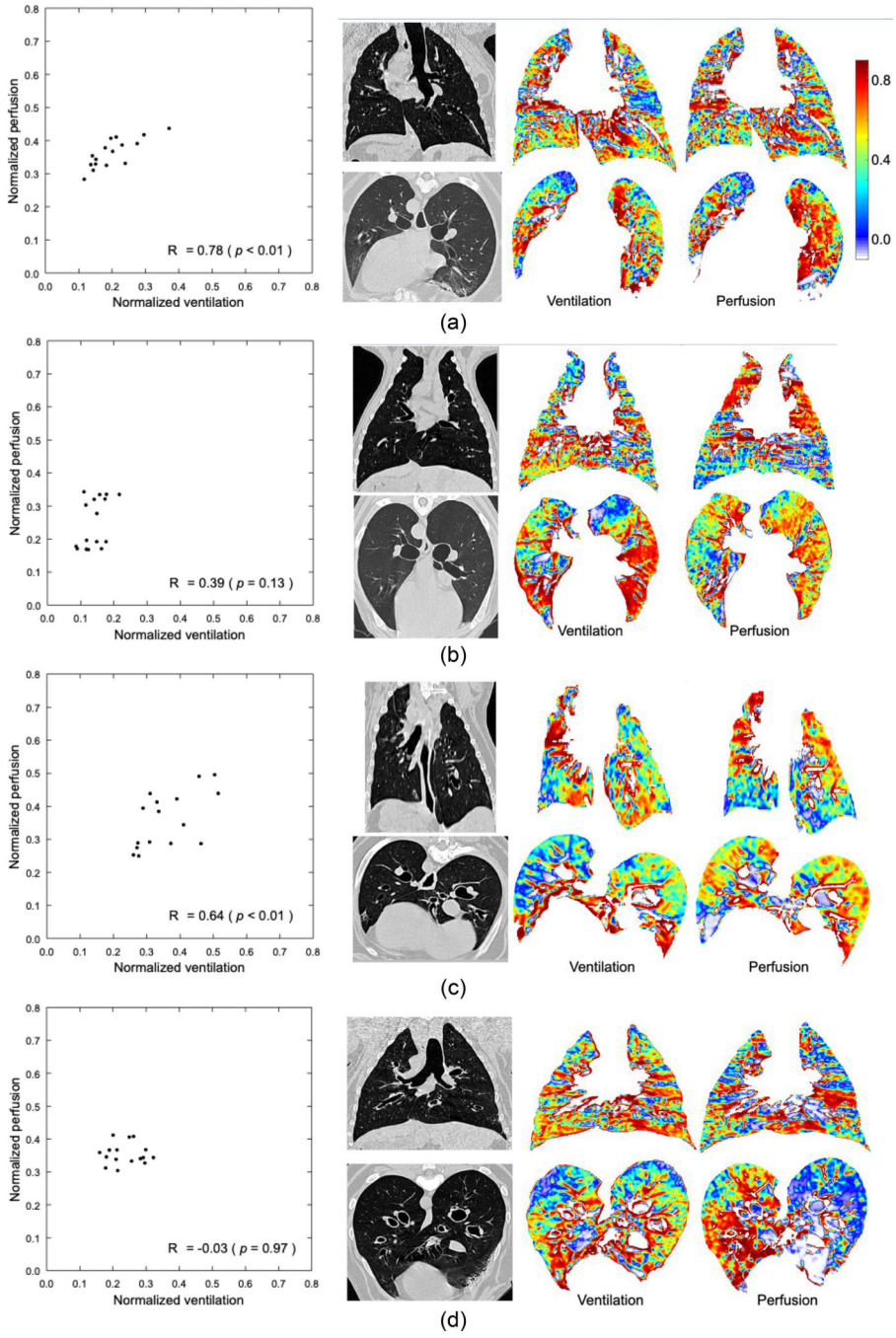

Fig 3.

Comparisons of ventilation and perfusion images as well as scatter plots based on 16 ROIs for four representative subjects: two normal subjects with (a) strong correlation (subject N1) and (b) moderate correlation (subject N2); and two diseased subjects with (c) strong correlation (subject D1, interstitial pneumonia) and (d) weak correlation (subject D2, bronchointerstitial pneumonia). Each data point represents the mean normalized ventilation or perfusion value within each of the 16 ROIs. R represents the Spearman's correlation coefficient.

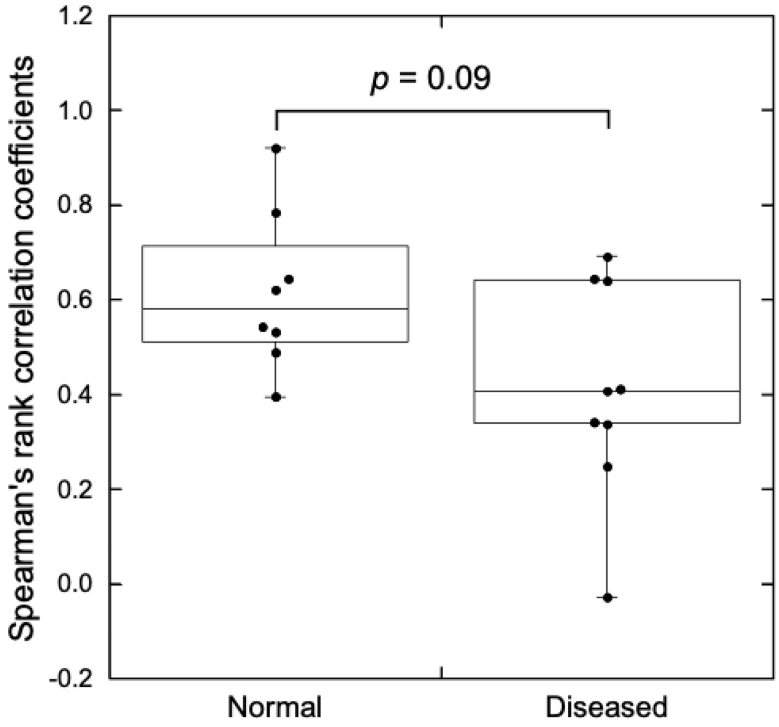

Fig 4.

Box plot of Spearman's rank correlation coefficients between ventilation and perfusion based on 16 ROIs (defined by dividing the lungs) for the normal and diseased lung groups. The central mark on each box represents the median, while the bottom and top edges indicate the 25th and 75th percentiles, respectively. Data points overlaid on the box plot represent individual subjects.

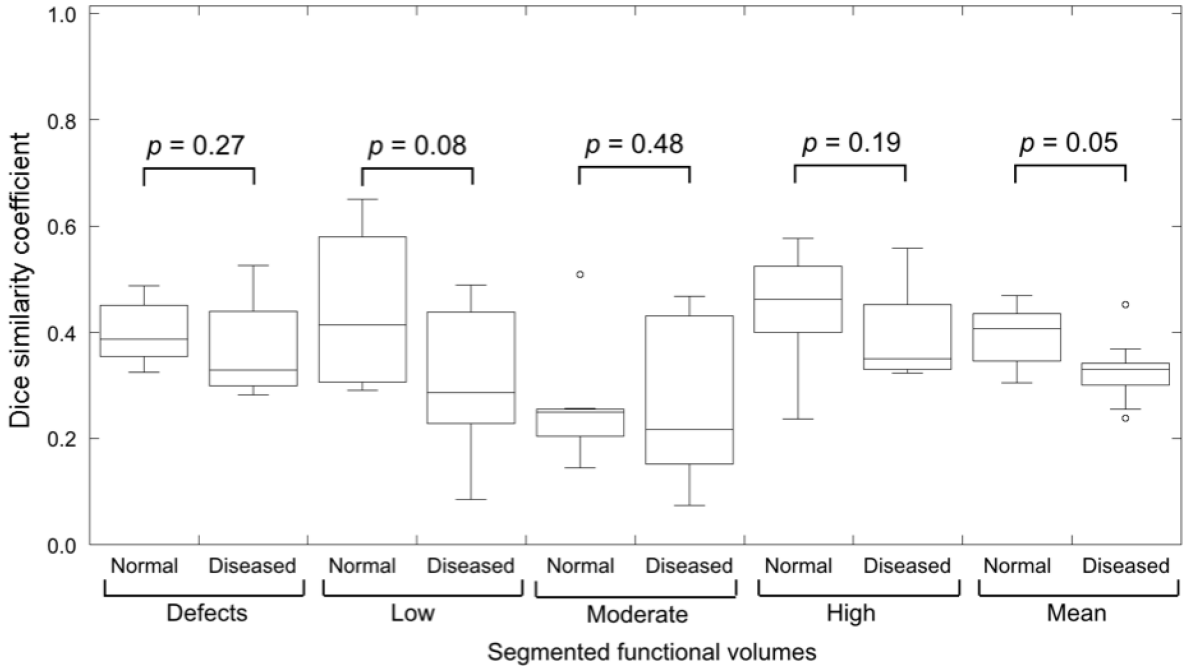

Fig 5.

Box plots of DSCs for the spatial overlap of four segmented functional volumes (defect, and low-, moderate-, and high-functional volumes) between ventilation and perfusion for the normal and diseased lung groups. The central mark on each box represents the median, while the bottom and top edges indicate the 25th and 75th percentiles, respectively.

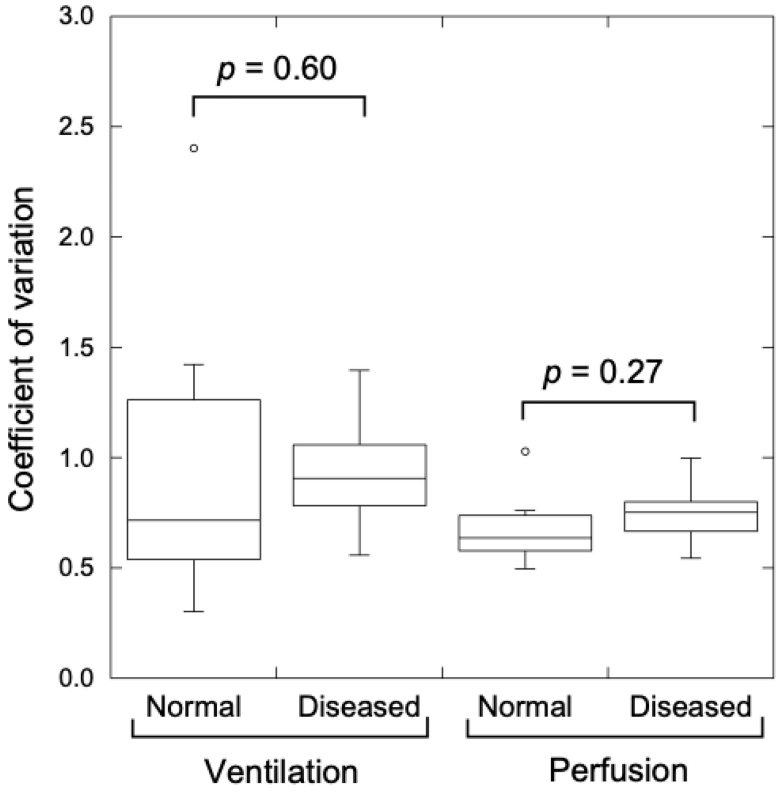

Fig 6.

Box plots of the CoVs of ventilation and perfusion for the normal and diseased lung groups. The central mark on each box represents the median, while the bottom and top edges indicate the 25th and 75th percentiles, respectively.

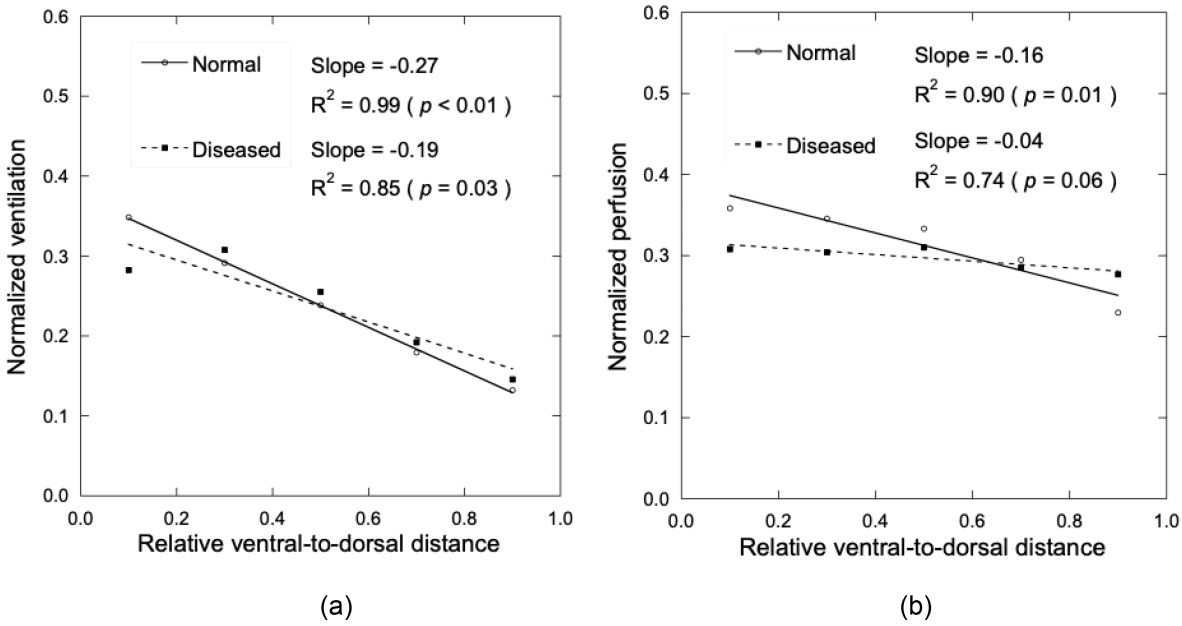

Fig 7.

Ventral-to-dorsal gradients of (a) ventilation and (b) perfusion for two representative subjects: subjects N1 (normal, solid lines) and D2 (diseased, dashed lines). The linear regression slope and coefficient (R^2) are shown.

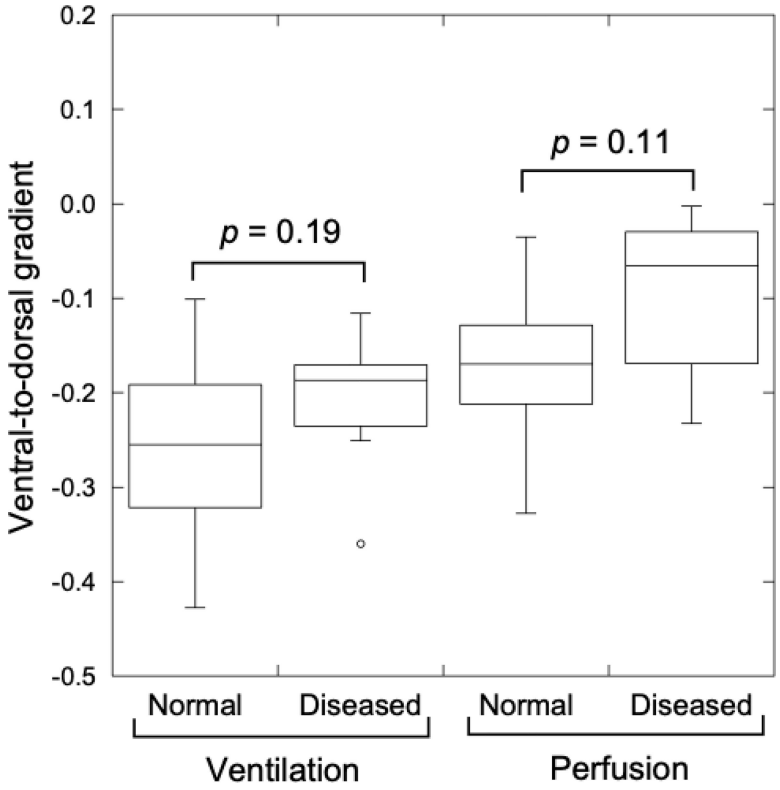

Fig 8.

Box plots of ventral-to-dorsal gradients (linear regression slopes) of ventilation and perfusion for the normal and diseased lung groups. The central mark on each box represents the median, while the bottom and top edges indicate the 25th and 75th percentiles, respectively.

Table 1.

Summary of previous studies on ventilation-perfusion matching, spatial heterogeneity, and gravitationally directed gradients.

Study	Modality	Subjects	Key finding
		Ventilation-perfusion matching	
Robertson *et al.*(1997)	FMS	5 normal pigs	Moderate to strong correlation (range 0.53–0.89) between V and Q
Altemeier*et al.*(1998)	FMS	5 normal pigs	Moderate to strong correlation (mean 0.89, range 0.76–0.95) between V and Q; After embolization, correlation decreased to 0.67 (range 0.57–0.74)
Altemeier*et al.*(2000)	FMS	6 normal pigs	Moderate to strong correlation (range 0.62–0.87) between V and Q
Melsom*et al.*(1997)	RMS	5 normal goats	Moderate to strong correlation (mean 0.81, range 0.68–0.87) between V and Q
Vidal Melo *et al.*(2000)	PET	6 normal volunteers	Greater V/Q heterogeneity ($p < 0.05$) in COPD
		10 COPD patients	
Suga *et al.*(2010)	SPECT	12 normal controls	Greater V/Q heterogeneity ($p < 0.01$) in emphysema
		38 PE patients	
Sando *et al.*(1997)	SPECT	10 normal volunteers 7 PVD, 9 PE, 18 BC, and 12 miscellaneous disease patients	Greater V/Q heterogeneity ($p < 0.01$) in PVD, PE, and BC
Yuan *et al.*(2011)	SPECT	51 NSCLC patients	39 % of patients had high V/Q mismatched areas
Ogawa *et al.*(1997)	Planar scintigraphy	40 ILD patients	49 % of patients had high V/Q mismatched areas V/Q matched defects were seen in 56%
Hwang *et al.*(2016)	Dual energy CT	52 COPD patients	Normal lung parenchyma showed a matched V/Q pattern;bronchial wall thickening showed a reversed mismatched V/Q ratio pattern (no quantitative data)
		Spatial heterogeneity	
Tzeng *et al.*(2009)	MRI	6 normal volunteers	Higher V heterogeneity ($p = 0.08$) in asthmatics
		10 asthmatic patients	
Vidal Melo *et al.*(2010)	PET	6 normal volunteers	Higher heterogeneity of V ($p < 0.01$) and Q ($p < 0.01$) in COPD
		10 COPD patients	
		Gravitationally directed gradients	
Vidal Melo *et al.*(2010)	PET	6 normal volunteers	Higher V gradient ($p < 0.05$) in normal subjects;
		10 COPD patients	Nonsignificant difference in Q gradient
Petersson*et al.* (2007)	SPECT	8 normal volunteers	V and Q gradients different from zero ($p < 0.05$)
Bauman *et al.*(2011)	MRI and SPECT/CT	7 normal pigs	V and Q gradients confirmed with both modalities in all animals (no quantitative data)

Abbreviations: V = ventilation, Q = perfusion, FMS = fluorescent microspheres, RMS = radioactive microspheres, BC = bronchogenic carcinoma, NSCLC = non-small-cell lung carcinoma, PE = pulmonary emphysema, ILD = interstitial lung disease, COPD = chronic obstructive pulmonary disease, PVD = pulmonary vascular disease, PFT = pulmonary functional test.